



## Practice article

# Improved cascaded model-free predictive speed control for PMSM speed ripple minimization based on ultra-local model

Zheng Sun<sup>a,b</sup>, Yongting Deng<sup>a,\*</sup>, Jianli Wang<sup>a,b</sup>, Hongwen Li<sup>a</sup>, Haiyang Cao<sup>a,b</sup>

<sup>a</sup> Changchun Institute of Optics, Fine Mechanics and Physics, Chinese Academy of Science, Changchun, Jilin 130033, China

<sup>b</sup> The University of Chinese Academy of Sciences, Beijing 100049, China

## ARTICLE INFO

## Keywords:

Model-free  
Predictive speed control  
Predictive current control  
PMSM  
Robustness

## ABSTRACT

This paper presents an improved cascaded model-free predictive speed and current control with the periodic and aperiodic disturbances suppression to achieve a smooth speed. The cascaded structure has an external speed loop and an internal current loop, both implemented with model-free predictive control to enhance the robustness of the controller. The current loop is designed based on the finite control set model-free predictive current control (FCS-MFPCC) strategy with an ultra-local model to regulate the stator currents, and the speed loop uses the proposed continuous control set model-free predictive speed control (CCS-MFPSC) to make full use of the excellent dynamic performance of the current-loop controller. To suppress the periodic disturbance that exists in the PMSM system, an improved parallel quasi-resonant controller (QRC) with an error limitation is embedded into the CCS-MFPSC, which can generate the compensated current. Based on the stability condition, the stability of the proposed MFPSC-QRC strategy is directly analyzed in the z-domain. Finally, the effectiveness and feasibility of the proposed cascaded model-free predictive speed and current strategy are validated on a PMSM test platform.

## 1. Introduction

Permanent magnet synchronous motor (PMSM) has been extensively implemented in aerospace, cutting-edge servo systems, and other fields benefiting from their remarkable characteristics such as superior torque inertia ratio, high efficiency, and excellent environmental adaptability. For a high-precision system, an outstanding speed-tracking performance is required [1–3]. However, the periodic and aperiodic disturbances in the PMSM control system will cause motor speed fluctuation, which may reduce the speed tracking accuracy. Meanwhile, the PMSM control system is a typical strong-coupling, multivariable, and nonlinear system. Therefore, a high-performance control strategy is required to achieve an excellent PMSM control system [4].

Over the last few decades, benefiting from the rapid development of microelectronics and computing power for the hardware platform, MPC that is suitable for multivariate and nonlinear systems has attracted the interest of scholars. The MPC can be regarded as an optimization problem. Based on the switching frequency, MPC applied in power electronics can be classified into the finite control set MPC (FCS-MPC) and continuous control set MPC (CCS-MPC) [5]. FCS-MPC can directly determine the optimal switching states of the converter that has a

discrete nature by calculating all the possible results. In contrast, CCS-MPC derives the optimal control actuation by solving an optimization problem. In [6], these two methods were compared, and they exhibited similar dynamic behaviors. However, compared with CCS-MPC, FCS-MPC may have a higher computational burden.

Whether for the FCS-MPC or CCS-MPC, the motor parameters will be directly applied to predict the future variables, which will cause a prediction error if the parameters mismatch between the nominal values and actual values [7]. Therefore, it is essential to enhance the robustness of the controller. In [8,9], online and offline identification methods are studied to identify the applied parameters, which can be directly revised. In addition, observer-based compensation strategies, such as disturbance observer (DOB) and extended state observer (ESO) [10], are proposed in [11] to observe the predicted error caused by parameters mismatch. In addition to the aforementioned methods, a data-driven model-free predictive current control (FCS-MFPCC) method is proposed in [12,13]. The FCS-MFPCC strategy can predict the future current based on a look-up table without directly applying the parameters and PMSM model, which can weaken the effect of parameter mismatch. In [14], an ultra-local model is studied to update the look-up table in the FCS-MFPCC. The model-free strategy provides a new idea

\* Corresponding author.

E-mail addresses: [sunzheng19@mails.ucas.ac.cn](mailto:sunzheng19@mails.ucas.ac.cn) (Z. Sun), [dengyongting@ciomp.ac.cn](mailto:dengyongting@ciomp.ac.cn) (Y. Deng), [wangjianli@ciomp.ac.cn](mailto:wangjianli@ciomp.ac.cn) (J. Wang), [lihongwen@ciomp.ac.cn](mailto:lihongwen@ciomp.ac.cn) (H. Li), [caohaiyang20@mails.ucas.ac.cn](mailto:caohaiyang20@mails.ucas.ac.cn) (H. Cao).

<https://doi.org/10.1016/j.isatra.2023.10.008>

Received 12 April 2023; Received in revised form 10 October 2023; Accepted 10 October 2023

Available online 12 October 2023

0019-0578/© 2023 ISA. Published by Elsevier Ltd. All rights reserved.

to overcome the reliance on motor parameters without increasing the complexity of the controller.

An outstanding advantage of the MPC is its excellent dynamic performance. However, there exist periodic and aperiodic disturbances in the PMSM control system, which will cause speed and current fluctuations. Therefore, to ensure the performance of the MPC controller at a steady state, it is necessary to suppress the aperiodic and periodic disturbances. For the aperiodic disturbance, common suppression methods include feedforward compensation and observer, such as sliding mode control and ADRC. According to the designed extended state observer (ESO) or sliding mode observer (SMO), the aperiodic disturbance will be online observed. Then, the estimated disturbance will be embedded into the controller to suppress the aperiodic disturbance [15]. However, because of the limited bandwidth, periodic disturbance may not be observed effectively by the observer. Therefore, to suppress the periodic disturbance, considerable efforts have been made in [16–19]. One of them is to modify the observer. In [16], an iterative learning method is applied with a disturbance observer to modify the gain of the observer. Besides, a periodic disturbance observer (PDOB) is proposed in [17], which can compensate for the periodic signal by embedding a time-delay link into a disturbance observer. Apart from the aforementioned methods, some advanced controllers, such as repetitive control [18], resonant control [19], and so on, have been researched to compensate for the periodic disturbance. The repetitive control [18] can improve the tracking accuracy by introducing the previous period deviation into the subsequent control period. In [19], a resonant controller that can increase the gain at fundamental and harmonic frequencies is applied to generate the compensated current to suppress the period disturbance. Generally, the aperiodic and periodic disturbances will simultaneously influence the performance of the controller. Therefore, it is essential to suppress the periodic and aperiodic disturbances simultaneously.

For a linear cascaded control, since the response speed of the internal current loop is faster than that of the external speed loop, the speed loop must have a compromise on the bandwidth to guarantee that the bandwidth of the speed loop is smaller than that of the current loop [20]. In [14], the FCS-MFPCC strategy is applied in the current loop to regulate the stator currents, and the reference current can be effectively tracked. However, the dynamic performance of the control system is still influenced by a classical PI controller. To make full use of the outstanding dynamic performance of the MPC, an improved cascaded model-free predictive speed and current control strategy is studied in this paper. The internal current loop is designed based on the FCS-MFPCC strategy to regulate the stator currents, and the external speed loop uses the proposed continuous control set model-free predictive speed control (CCS-MFPSC) to fast respond to the speed and load change. Furthermore, an ESO that is applied to observe the lumped disturbance term of the ultra-local model can simultaneously suppress the aperiodic disturbance, and an improved parallel quasi-resonant controller (QRC) with an error limitation is inserted into the proposed CCS-MFPSC to suppress the periodic disturbance. The following is a summary of the main contributions.

- (1) An improved cascaded model-free predictive speed and current control strategy is proposed to take full advantage of the excellent dynamic performance for the MPC and get rid of the reliance on motor parameters, which can decrease the response time and speed overshoot.
- (2) A parallel QRC is embedded in the external speed loop to improve the speed tracking performance at a steady state, which can be used together with the designed ESO to simultaneously suppress the periodic and aperiodic disturbances.
- (3) To avoid the dynamic performance of the proposed CCS-MFPSC being affected, the action time of the embedded QRC is limited based on the speed tracking error.

The remainder of this paper is organized as follows. The PMSM mathematical model and torque ripple are analyzed in Sections Section 2. Section 3 elaborates the proposed cascaded model-free predictive speed and current control strategy. In Section 4, the validation of the stability and the parameters selection of the designed MFPC-QRC controller is presented. Section 5 presents the comparative experimental results to test the feasibility of the proposed cascaded model-free predictive control strategy. The conclusions are summarized in Section 6.

## 2. PMSM model and torque ripple analysis

In this section, the mathematical and dynamic models of the PMSM are established. In addition, torque ripple is briefly analyzed, and the dynamic model is rewritten by considering the periodic and aperiodic disturbances.

### 2.1. PMSM model

In the rotating reference frame (dq-axis), the PMSM mathematical model can be expressed without considering the eddy currents and hysteresis loss as

$$\begin{bmatrix} u_d \\ u_q \end{bmatrix} = \begin{bmatrix} L_d & 0 \\ 0 & L_q \end{bmatrix} \begin{bmatrix} \dot{i}_d \\ \dot{i}_q \end{bmatrix} + \begin{bmatrix} R_s & -L_q n_p \omega_m \\ L_d n_p \omega_m & R_s \end{bmatrix} \begin{bmatrix} i_d \\ i_q \end{bmatrix} + \begin{bmatrix} 0 \\ n_p \omega_m \psi_f \end{bmatrix} \quad (1)$$

where  $\begin{bmatrix} i_d & i_q \end{bmatrix}^T$  denotes the matrix of the dq-axis stator current;  $\begin{bmatrix} u_d & u_q \end{bmatrix}^T$  denotes the matrix of the dq-axis stator voltage;  $\begin{bmatrix} L_d & L_q \end{bmatrix}^T$  denotes the matrix of the dq-axis inductance;  $n_p$  represents the number of pole pairs;  $R_s$  represents the stator resistance;  $\omega_m$  represents the rotor mechanical angular velocity and  $\psi_f$  represents the flux linkage.

Furthermore, the dynamic equation of PMSM can be written as

$$\frac{J}{n_p} \frac{d\omega_e}{dt} = T_e - T_L - \frac{B}{n_p} \omega_e \quad (2)$$

where  $\omega_e$  denotes the rotor electrical angular velocity;  $J$  denotes the rotational inertia;  $B$  denotes the friction coefficient;  $T_L$  denotes the load torque;  $T_e$  represents the electromagnetic torque of the PMSM. The equation of  $T_e$  can be expressed as

$$T_e = \frac{3}{2} n_p i_q [\psi_f + (L_d - L_q) i_d]. \quad (3)$$

### 2.2. Torque ripple analysis

One of the goals of a PMSM control system is to achieve a smooth speed. However, the disturbances that exist in the control system will cause the speed to fluctuate, which will enlarge the speed tracking error. Based on the disturbance generation mechanism, the disturbances in the speed loop can be divided into periodic and aperiodic disturbances. The main aperiodic disturbances can be divided into three categories: friction torque, parameters mismatch, and load torque [21]. In addition, the main periodic disturbance is caused by the current sampling error that consists of the scaling errors and direct current (DC) offset. Because the stator current and voltage are measured by the sensors, the scaling errors and DC offset that exist in the measurement system will oscillate the torque at different frequencies [22]. In addition to the current detection error, inverter nonlinearity, cogging torque, and magnetic flux harmonics also introduce higher harmonics [16]. Therefore, for a surface-mounted PMSM that satisfies  $L_d = L_q$ , the dynamic equation that considers the aperiodic and periodic disturbances can be revised as

$$\begin{aligned} \frac{(J + \Delta J)}{n_p} \frac{d\omega_e}{dt} &= T_e - T_L - \frac{(B + \Delta B)}{n_p} \omega_e \\ &= \frac{3}{2} n_p (\psi_f + \Delta\psi_f) i_q - T_L - \frac{(B + \Delta B)}{n_p} \omega_e + T_{eap} + T_{ep} \end{aligned} \quad (4)$$

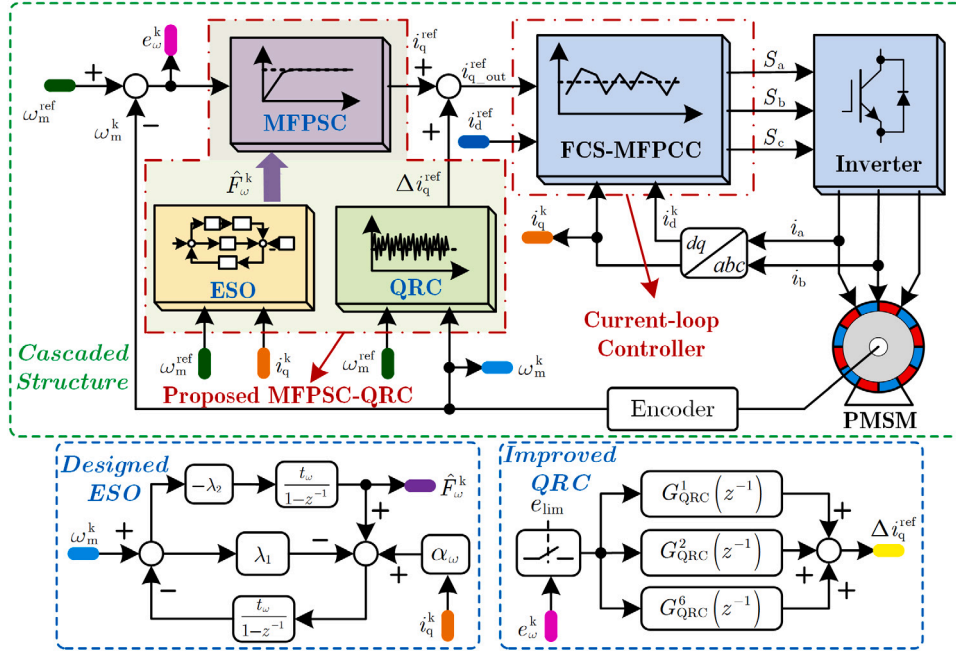


Fig. 1. Block diagram of the proposed cascaded model-free predictive control.

where  $\Delta J$  denotes the variation of the rotational inertia;  $\Delta\psi_f$  denotes the variation of the flux linkage;  $\Delta B$  denotes the variation of the friction coefficient;  $T_{eap}$  and  $T_{ep}$  represent the electromagnetic torque caused by the aperiodic disturbance and periodic disturbance, respectively.

In the PMSM drive system, the periodic torque ripples can be expressed as

$$T_{ep} = \frac{3}{2} n_p \left( \sum_{n=1}^{\infty} \psi_{6n} \cos(6n\theta_e) \right) \cdot (\Delta i_{vsi} + \Delta i_{sample}) + T_{cog} \quad (5)$$

where  $\psi_{6n}$  denotes the 6<sup>th</sup> harmonic amplitude of the motor flux;  $\theta_e$  is the motor electrical angle;  $\Delta i_{vsi}$  represents the current errors caused by the nonlinearity of the inverter;  $\Delta i_{sample}$  represents the current errors introduced by the current sampling; and  $T_{cog}$  represents the motor cogging torque. According to [16], the  $\Delta i_{vsi}$ ,  $\Delta i_{sample}$  and  $T_{cog}$  can be depicted as

$$\begin{cases} \Delta i_{vsi} = \frac{\omega_e}{\sqrt{R_s^2 + (6\omega_e L_s)^2}} \left[ -A_1 \cos(6\theta_e + \theta_5) + A_2 \cos(6\theta_e + \theta_7) + \frac{48V_{dead}}{35\omega_e\pi} \sin(6\theta_e) \right] \\ \Delta i_{sample} = \frac{2}{\sqrt{3}} \sqrt{\Delta i_a^2 + \Delta i_a \Delta i_b + \Delta i_b^2} \cdot \cos(\theta_e + \theta_1) + \frac{i_s}{\sqrt{3}} \left( \frac{k_a - k_b}{k_a k_b} \right) \\ \quad \times \left[ \cos\left(2\theta_e + \frac{\pi}{3}\right) + \frac{1}{2} \right] \\ T_{cog} = \sum_{n=1}^{\infty} T_{cog,n} \sin(n\eta\theta_e) \end{cases} \quad (6)$$

where  $A_1$  and  $A_2$  are the harmonics amplitudes;  $\theta_5$  and  $\theta_7$  are the initial phase;  $V_{dead}$  denotes the voltage variation that is affected by the dead-time;  $\Delta i_a$  and  $\Delta i_b$  denote the direct current (DC) bias of the a-phase current  $i_a$  and b-phase current  $i_b$ , respectively;  $\theta_1$  is an angle value that is associated with  $\Delta i_a$  and  $\Delta i_b$ .  $i_s$  denotes the phase current amplitude;  $k_a$  and  $k_b$  denote the scaling factors of the  $i_a$  and  $i_b$ ;  $\eta$  denote the least common multiple between the number of poles and slots; and  $T_{cog,n}$

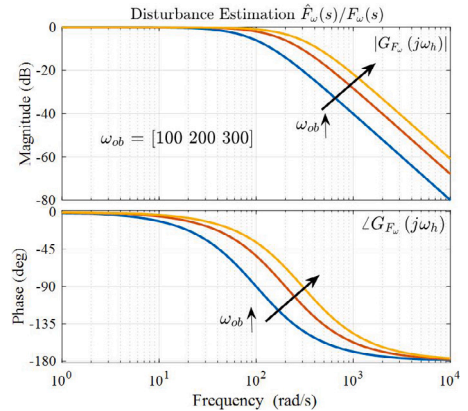


Fig. 2. Bode plot for the disturbance estimation with  $\omega_{ob} = [100 \ 200 \ 300]$ .

denote the harmonic amplitude of the  $n$ th cogging torque. According to (5) and (6), apart from the DC components, the torque ripples mainly include the 1st, 2nd, and 6th harmonic components.

### 3. Proposed cascaded control strategy

In this section, a cascade model-free predictive control strategy that consists of two main parts is described, as shown in Fig. 1. The cascaded structure mainly includes an external speed loop and an internal current loop. The external speed loop is applied to generate the reference current for the current loop, and the internal current loop can determine the optimal switching states according to the designed cost function. The details of the designed control strategy are elaborated in the next subsection.

#### 3.1. Internal current loop controller

For the current loop, the FCS-MFPCC strategy that is based on a look-up table (LUT) is applied. In Fig. 1, the modulator is not applied

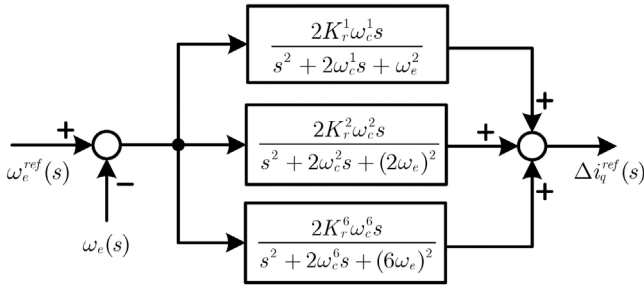


Fig. 3. The structure block diagram for the parallel QRC.

rather than directly generates the switching states that are generated by minimizing the cost function. In this case, the cost function is designed as

$$g_j = \left( i_{q,out}^{ref} - i_{qp}^{k+2} \Big|_j \right)^2 + \left( i_d^{ref} - i_{dp}^{k+2} \Big|_j \right)^2, \quad j = 0, \dots, 7 \quad (7)$$

where  $i_{q,out}^{ref}$  denotes the  $q$ -axis reference current that is generated from the external speed loop;  $i_d^{ref}$  denotes the  $d$ -axis reference current;  $i_{qp}^{k+2}$  and  $i_{dp}^{k+2}$  represent the  $dq$ -axis predicted currents at the  $(k + 2)$ th sampling period, and  $j$  represents the voltage number of the inverter.

In the FCS-MFPCC, the stator currents are predicted with a look-up table (LUT) that is applied to store the current variations. According to the LUT, the future currents are predicted as

$$\begin{cases} i_{sp}^{k+1} = i_s^k + \Delta i_{s,LUT} \Big|_{u_s^k} \\ i_{sp}^{k+2} \Big|_j = i_{sp}^{k+1} + \Delta i_{s,LUT} \Big|_{u_j} \end{cases} \quad (8)$$

where  $i_s = [i_d \quad i_q]^T$ ;  $i_s^k$  and  $u_s^k$  represent the sampling current and applied voltage vector at the  $(k+1)$ th sampling period, respectively;  $i_{sp}^{k+1}$  represents the predicted current at the  $(k)$ th sampling period;  $\Delta i_{s,LUT}$  and  $\Delta i_{s,LUT}^{k+1}$  denote the current variations corresponding to the voltage vectors, which are stored in the look-up table (LUT) [14].

Substituting (8) into (7), the cost function  $g_j$  of the all possible results will be calculated. Then, the optimal switching state (i.e., optimal voltage vector) will be determined by choosing the minimum cost function (7).

$$S_{opt} = \arg \min g(u_j) \quad (9)$$

where  $S_{opt}$  denotes the selected optimal switching states.

### 3.2. External speed loop controller

Here, the CCS-MFPSC strategy is proposed to track the reference speed without directly using motor parameters, which is considered as a replacement to the conventional PI controller. Meanwhile, an improved parallel quasi-resonant controller (QRC) with an error limitation is introduced into the CCS-MFPSC to suppress the periodic disturbance.

#### 3.2.1. CCS-MFPSC controller design

The proposed CCS-MFPSC controller is based on the PMSM dynamic model that is given in (2) and (4). Taking  $\omega_e$  and  $i_q$  as the output and input variables, the dynamic equation (4) with the lumped disturbance can be rewritten in the ultra-local model form [23] as

$$\frac{d\omega_m}{dt} = F_\omega + \alpha_\omega i_q \quad (10)$$

where  $F_\omega$  represents the lumped disturbance that includes parameters variation, periodic and aperiodic disturbances; and  $\alpha_\omega$  represents the optional scaling factor that can be designed by the designer.

To generate a more accurate  $q$ -axis reference current, a second-order Taylor expansion is applied to discretize the dynamic model (10), which is derived as

$$\begin{cases} \omega_m^{k+1} = \omega_m^k + \frac{d\omega_m}{dt} \cdot t_\omega + \frac{d^2\omega_m}{dt^2} \cdot \frac{t_\omega^2}{2} \\ \frac{d^2\omega_m}{dt^2} = \frac{di_q}{dt} \end{cases} \quad (11)$$

where  $\omega_m^k$  and  $\omega_m^{k+1}$  denote the mechanical angular velocity at the  $(k)$ th and  $(k + 1)$ th sampling period, respectively;  $t_\omega$  represents the speed-loop sampling period.

Substituting (10) into (11) and using the backward Euler transformation, the discrete-time dynamic model can be obtained. By replacing  $\omega_m^{k+1}$  and  $i_q^k$  with  $\omega_m^{ref}$  and  $i_q^{ref}$  in (11), the  $q$ -axis reference current is derived as

$$i_q^{ref} = \frac{2}{3\alpha_\omega t_\omega} (\omega_m^{ref} - \omega_m^k) - \frac{2}{3\alpha_\omega} \hat{F}_\omega^k + \frac{1}{3} i_q^{k-1} \quad (12)$$

where  $i_q^{ref}$  denotes the  $q$ -axis reference current;  $\hat{F}_\omega^k$  represents the estimated lumped disturbance at the  $(k)$ th sampling period;  $i_q^{k-1}$  denotes the  $q$ -axis current at the  $(k - 1)$ th sampling period.

Furthermore, to obtain the unknown disturbance and avoid directly using the motor parameters, a discrete-time ESO is designed to observe the lumped disturbance  $\hat{F}_\omega^k$ . Taking  $\omega_m$  and  $i_q$  in (10) as state variables and applying the first-order backward Euler transformation, i.e.  $\hat{\omega}_m = \frac{\omega_m^k - \omega_m^{k-1}}{t_\omega}$  and  $\hat{F}_\omega = \frac{F_\omega^k - F_\omega^{k-1}}{t_\omega}$ , the discrete-time ESO is designed as

$$\begin{cases} e_\omega^k = \hat{\omega}_m^k - \omega_m^k \\ \hat{\omega}_m^k = \hat{\omega}_m^{k-1} + t_\omega [\hat{F}_\omega^k + \alpha_\omega i_q^k - \lambda_1 e_\omega^k] \\ \hat{F}_\omega^k = \hat{F}_\omega^{k-1} - t_\omega \lambda_2 e_\omega^k \end{cases} \quad (13)$$

where  $\hat{\omega}_m^{k-1}$  and  $\hat{\omega}_m^k$  denote the observed mechanical angular velocity at the  $(k - 1)$ th and  $(k)$ th sampling period, respectively;  $e_\omega^k$  denotes the observed error of the mechanical angular velocity at the  $(k)$ th sampling period; and  $\hat{F}_\omega^{k-1}$  represents the observed lumped disturbance at the  $(k - 1)$ th sampling period; and  $\lambda_1$  and  $\lambda_2$  are the gain coefficients for the designed ESO. Normally, the  $\lambda_1$  and  $\lambda_2$  follow the equation that  $\lambda_1 = 2\omega_{ob}$  and  $\lambda_2 = \omega_{ob}^2$  [24], where  $\omega_{ob}$  represents the bandwidth of the designed ESO. According to (13), the designed ESO can estimate the lumped disturbance  $\hat{F}_\omega^k$ . Substituting  $\hat{F}_\omega^k$  into (12), the  $q$ -axis reference current will be derived.

#### 3.2.2. MFPSC-QRC controller design

In the proposed CCS-MFPSC strategy, multiple disturbances are denoted as a lumped disturbance that is estimated by the designed ESO. However, Fig. 2 shows that the high-frequency periodic disturbance may lost because of the limited passing frequency. Therefore, to achieve a smooth speed, a compensation method is necessary to suppress the periodic disturbances in (5). According to (5), the torque ripples mainly include the 1st, 2nd, and 6th harmonic components. Therefore, to reduce the torque ripples, a parallel QRC for the harmonics is designed as

$$\begin{aligned} G_{QRC}(s) &= G_{QRC}^1(s) + G_{QRC}^2(s) + G_{QRC}^6(s) \\ &= \sum_{m=1,2,6} \frac{2K_r^m \omega_c^m s}{s^2 + 2\omega_c^m s + (m\omega_e)^2} \end{aligned} \quad (14)$$

where  $m = 1, 2, 6$  means the 1st, 2nd and 6th harmonic components;  $\omega_c^m$  denotes the  $m$ th cutoff frequency; and  $K_r^m$  denotes the  $m$ th resonant coefficient. Based on (4) to (6), the period of the periodic disturbance is associated with the electrical angle of the motor. Therefore, the resonant frequencies of the designed QRC are the  $m$ th electrical angular velocity to suppress the periodic disturbance.

Fig. 3 shows the structure diagram of the parallel QRC. Because the three QRCs have similar structures, we can calculate the 1st, 2nd, and

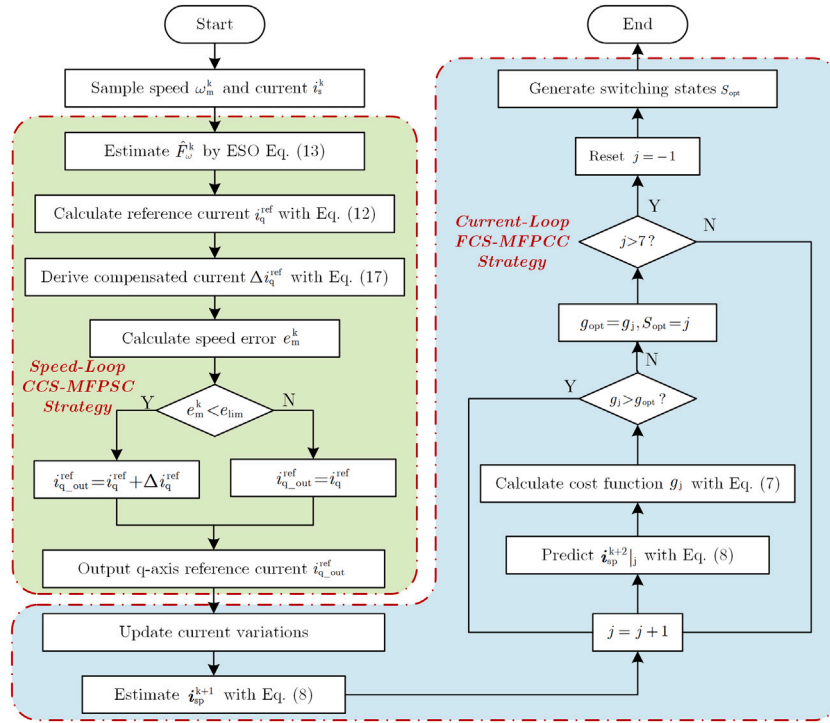


Fig. 4. The flowchart of the proposed cascaded model-free predictive control strategy.

6th harmonic components separately and add them together. Taking  $G_{\text{QRC}}^1(s)$  as an example, based on the Tustin transform, i.e.,  $s = \frac{2}{T} \frac{1-z^{-1}}{1+z^{-1}}$ , the discrete-time transform function for the  $G_{\text{QRC}}^1(s)$  can be derived as

$$G_{\text{QRC}}^1(z) = \frac{4K_t^1 \omega_c^1 t_\omega (1-z^{-2})}{(4+4\omega_c^1 t_\omega + \omega_c^2 t_\omega^2) + (2\omega_c^2 t_\omega^2 - 8)z^{-1} + (4-4\omega_c^1 t_\omega + \omega_c^2 t_\omega^2)z^{-2}} \quad (15)$$

Next, the discrete-time transform function  $G_{\text{QRC}}^2(z)$  and  $G_{\text{QRC}}^6(z)$  can be derived with a similar method. Therefore, the discrete-time transform function of the applied QRC can be calculated as

$$G_{\text{QRC}}(z) = G_{\text{QRC}}^1(z) + G_{\text{QRC}}^2(z) + G_{\text{QRC}}^6(z) \quad (16)$$

For the designed parallel QRC, the input variable is the speed tracking error, and the output variable is the compensated current to minish the torque ripples. Therefore, based on the discrete-time transform functions (15) and (16), the compensated current can be calculated as

$$\Delta i_q^{\text{ref}} = [\omega_e^{\text{ref}} - \omega_e^k] [G_{\text{QRC}}^1(z) + G_{\text{QRC}}^2(z) + G_{\text{QRC}}^6(z)] \quad (17)$$

where  $\omega_e^{\text{ref}}$  denotes the reference electrical angular velocity;  $\omega_e^k$  denotes the motor electrical angular velocity at the  $(k)$ th sampling period. Finally, considering the periodic disturbance, the  $q$ -axis reference current can be revised by combining (17) and (12) as

$$i_{q,\text{out}}^{\text{ref}} = i_q^{\text{ref}} + \Delta i_q^{\text{ref}} \quad (18)$$

where  $i_{q,\text{out}}^{\text{ref}}$  represents the revised  $q$ -axis reference current.

To ensure the security of the hardware system, a limitation on the revised reference current is necessary to avoid an excessive current that will destroy the hardware platform. The limitation is set as

$$i_{q,\text{out}}^{\text{ref}} = \begin{cases} -i_q^{\text{lim}}, & i_{q,\text{out}}^{\text{ref}} < -i_q^{\text{lim}} \\ i_{q,\text{out}}^{\text{ref}}, & -i_q^{\text{lim}} \leq i_{q,\text{out}}^{\text{ref}} \leq i_q^{\text{lim}} \\ i_q^{\text{lim}}, & i_{q,\text{out}}^{\text{ref}} > i_q^{\text{lim}} \end{cases} \quad (19)$$

where  $i_q^{\text{lim}}$  denotes the limitation for the output reference current.

For a QRC, because the resonant controller involves two integrators [25], a large speed error will be accumulated when the motor starts, and wind-up problem will appear, which will cause speed overshoot. Therefore, to decrease the overshoot of the speed and avoid the dynamic performance being influenced, a judgment condition is set to limit the input value of the QRC, i.e. speed tracking error. If the speed error  $e_m^k$  ( $e_m^k = \omega_m^{\text{ref}} - \omega_m^k$ ) is larger than the limitation  $e_{\text{lim}}$ , the designed QRC will not operate and the  $q$ -axis reference current will be derived from (12). Meanwhile, if the speed error  $e_m^k$  is less than the limitation  $e_{\text{lim}}$ , the designed QRC will generate a compensated current in (18). To elaborate on the proposed method more clearly, Fig. 4 exhibits the flowchart of the proposed cascaded model-free predictive control strategy. In the flowchart, the  $g_{\text{opt}}$  denotes the minimum cost function.

#### 4. Stability analysis and parameters configuration

##### 4.1. Stability analysis of the designed MFPS-C-QRC controller

This section analyzes the stability of the designed MFPS-C-QRC controller by simplifying the closed-loop system as an equivalent unity-feedback system. Based on the shift operator ( $z^{-1}$ ), we can combine the target information from different sampling periods. According to (13), if we eliminate the speed estimated error  $e_\omega^k$ , the selected state variables will be expressed as

$$\begin{cases} \omega_m^k = \frac{2t_\omega \omega_{\text{ob}} (1-z^{-1}) + t_\omega^2 \omega_{\text{ob}}^2}{(1-z^{-1} + t_\omega \omega_{\text{ob}})^2} \cdot \omega_m^k + \frac{t_\omega \alpha_\omega (1-z^{-1})}{(1-z^{-1} + t_\omega \omega_{\text{ob}})^2} \cdot i_q^k \\ \hat{F}_\omega^k = \frac{(1-z^{-1}) t_\omega \omega_{\text{ob}}^2}{(1-z^{-1} + t_\omega \omega_{\text{ob}})^2} \cdot \omega_m^k - \frac{t_\omega^2 \omega_{\text{ob}}^2 \alpha_\omega}{(1-z^{-1} + t_\omega \omega_{\text{ob}})^2} \cdot i_q^k \end{cases} \quad (20)$$

Similarly, based on the (12) and (16), the relationship between the motor speed  $\omega_m^k$  and  $q$ -axis current  $i_q^k$  is expressed as

$$\left(1 - \frac{1}{3}z^{-1}\right) i_q^k = \left[\frac{2}{3\alpha_\omega t_\omega} + G_{\text{QRC}}(z)\right] \cdot (\omega_m^* - \omega_m^k) - \frac{2}{3\alpha_\omega} \cdot \hat{F}_\omega^k \quad (21)$$

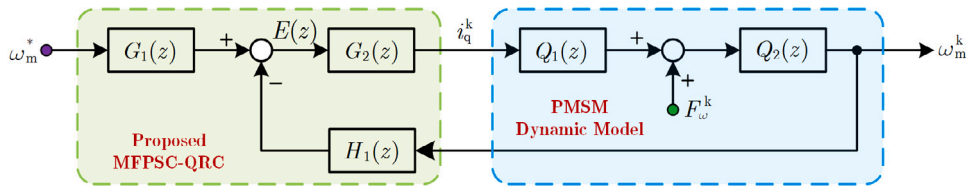


Fig. 5. Block diagram of the closed-loop system with the proposed MFPS-C-QRC.

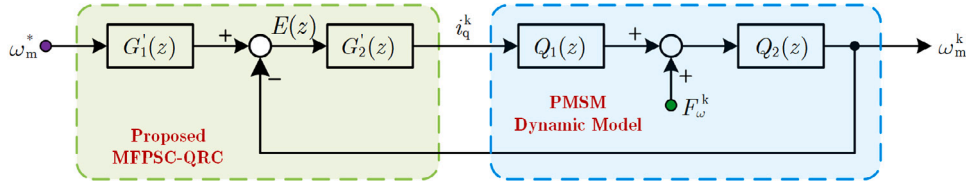


Fig. 6. Block diagram of the equivalent unity-feedback closed-loop system with the proposed MFPS-C-QRC.

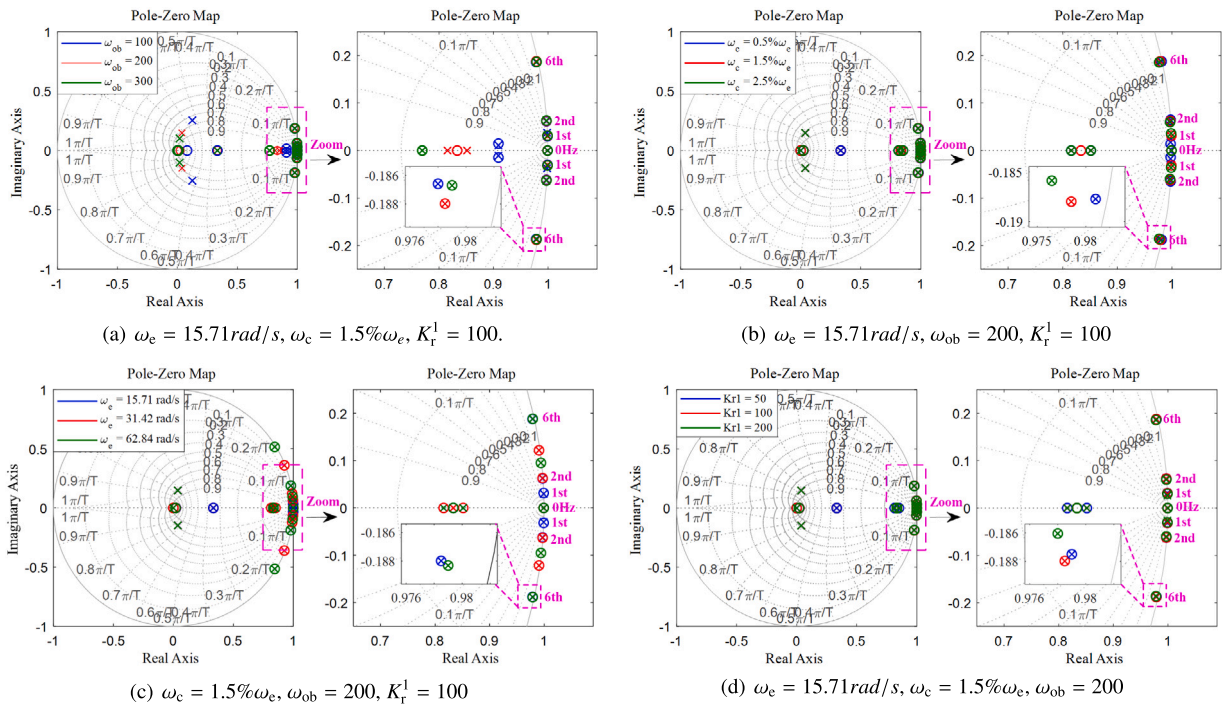


Fig. 7. Pole-zero map and impulse response of the closed-loop discrete-time system with the proposed MFPS-C-QRC. (For interpretation of the references to color in this figure legend, the reader is referred to the web version of this article.)

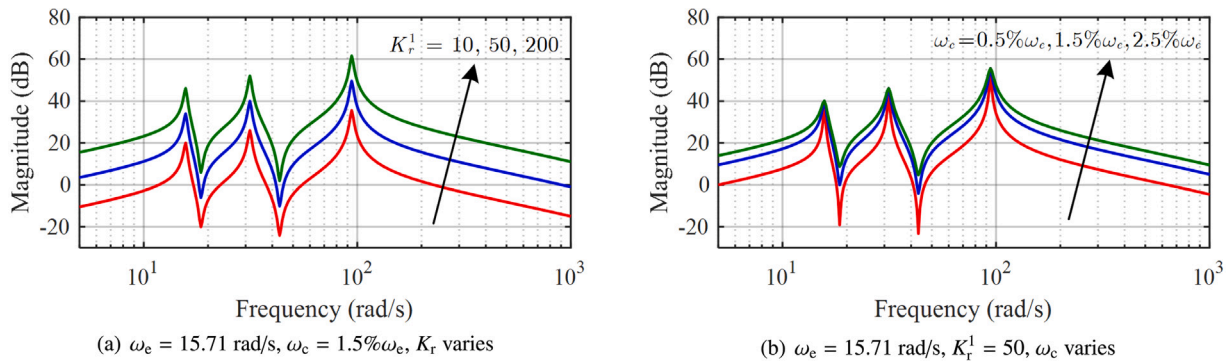
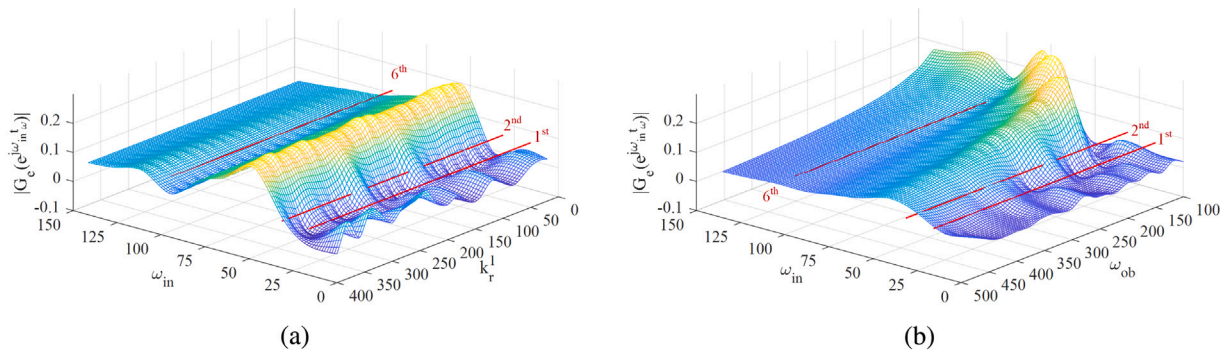


Fig. 8. Bode plot of the designed with varying parameters.



**Fig. 9.** Absolute value  $|G_e(e^{jm\omega_{in}t\omega})|$  with varying parameters. (a)  $\omega_e = 15.71$  rad/s,  $\omega_c = 1.5\omega_e$ ,  $\omega_{ob} = 200$ ,  $K_r$  varies from 20 to 400; (b)  $\omega_e = 15.71$  rad/s,  $\omega_c = 1.5\omega_e$ ,  $K_r^1 = 100$ ,  $\omega_{ob}$  varies from 100 to 500. (For interpretation of the references to color in this figure legend, the reader is referred to the web version of this article.)

In (20), the lumped disturbance  $\hat{F}_\omega^k$  can be calculated. Then, substituting (20) into (21), the  $i_q^k$  can be derived as

$$\begin{cases} i_q^k = G_2(z) \cdot [G_1(z) \cdot \omega_m^* - H_1(z) \cdot \omega_m^k] \\ G_1(z) = \frac{2}{3\alpha_\omega t_\omega} + G_{\text{QRC}}(z) \\ H_1(z) = G_1(z) + \frac{2}{3\alpha_\omega} \cdot \frac{(1-z^{-1})t_\omega \omega_{ob}^2}{(1-z^{-1} + t_\omega \omega_{ob})^2} \\ G_2(z) = \frac{1}{1 - \frac{1}{3}z^{-1} - \frac{2}{3} \cdot \frac{t_\omega^2 \omega_{ob}^2}{(1-z^{-1} + t_\omega \omega_{ob})^2}} \end{cases} \quad (22)$$

According to (22), the block diagram of the speed closed-loop system is depicted in Fig. 5. Because the designed MFPS-C-QRC controller is implemented on the discrete-time hardware platform, current and speed information need to be sampled from the sampler. Therefore, we can simplify the speed closed-loop system to an equivalent unity-feedback closed-loop system, as shown in Fig. 6.

In Fig. 6,  $G'_1(z)$ ,  $G'_2(z)$ ,  $Q_1(z)$  and  $Q_2(z)$  can be expressed as

$$\begin{cases} G'_1(z) = \frac{G_1(z)}{H_1(z)} = \frac{\Delta_1(z^{-1}) [2 + 3\alpha_\omega t_\omega G_{\text{QRC}}(z)]}{\Delta_1(z^{-1}) [2 + 3\alpha_\omega t_\omega G_{\text{QRC}}(z)] + 2(1-z^{-1})t_\omega^2 \omega_{ob}^2} \\ G'_2(z) = G_2(z) H_1(z) \\ = \frac{1}{\alpha_\omega t_\omega} \cdot \frac{2\Delta_1(z) + 3\alpha_\omega t_\omega G_{\text{QRC}}(z) \Delta_1(z) + 2(1-z^{-1})t_\omega^2 \omega_{ob}^2}{3\Delta_1(z) - z^{-1}\Delta_1(z) - 2t_\omega^2 \omega_{ob}^2} \\ Q_1(z) = \alpha_\omega t_\omega \left( \frac{3}{2} - \frac{1}{2}z^{-1} \right) \\ Q_2(z) = \frac{1}{1-z^{-1}} \end{cases} \quad (23)$$

where  $\Delta_1(z) = (1 - z^{-1} + t_\omega \omega_{ob})^2$ .

Based on Fig. 6, the pulse transfer function for the closed-loop discrete-time system is written as

$$G_{\text{PC}}(z) = \frac{G'_2(z) Q_1(z) Q_2(z)}{1 + G'_2(z) Q_1(z) Q_2(z)} \quad (24)$$

For a discrete-time system, the sufficient and necessary condition to be stable is that the poles of the closed-loop system are all located in a unit circle of the  $z$ -plane. The pole-zero map of the closed-loop discrete-time system with the proposed MFPS-C-QRC is shown in Fig. 7. Because a parallel quasi-resonant controller is embedded into the designed MFPS-C controller, the corresponding frequencies are involved in the pole-zero map to suppress the periodic disturbance, as the pink markers in Fig. 7. Furthermore, the poles of the closed-loop system are all distributed in the unit circle. Therefore, a conclusion is drawn that the proposed closed-speed system is stable.

#### 4.2. Parameters configuration

It can be seen from (23) and Fig. 7 that the stability of the discrete-time system is associated with three parameters:  $\omega_{ob}$ ,  $K_r^m$  ( $K_r^1$ ,  $K_r^2$ ,  $K_r^6$ ), and  $\omega_c^m$  ( $\omega_c^1$ ,  $\omega_c^2$ ,  $\omega_c^6$ ). According to [1], because the torque ripples at low speed will be more pronounced than at high speed, the resonant frequency  $\omega_e$  is set to 15.71 rad/s. Fig. 8 shows the bode plot of the designed QRC with  $K_r$  varies (a) and  $\omega_c$  varies (b). In Fig. 8(a), the gain of the designed QRC that closes to the resonant frequency will arise with the increased  $K_r$ . However, the signal around the resonant frequency will be amplified with an overlarge  $K_r$ , which will influence the performance of the harmonics suppression. Meanwhile, Fig. 8(b) shows that the gain near the resonant frequency can be adjusted by selecting a proper  $\omega_c$ . According to [26], a larger  $k_r$  should be set with the resonant frequency increases. Therefore, the values of  $k_r^2$  and  $k_r^6$  are set to  $2k_r^1$  and  $6k_r^1$ , respectively. Then, the gain around the resonant frequency can be decreased by adjusting  $\omega_c$ . In our study, the  $\omega_c^m$  is selected to 1.5% ( $m\omega_e$ ). Besides,  $\omega_{ob}$  is an important parameter to observe the lumped disturbance in the ultra-local model. Therefore,  $\omega_{ob}$  can be designed to be slightly larger to guarantee that the designed ESO can effectively track the lumped disturbance.

To evaluate the effectiveness of the selected parameters, an approach that is based on the pulse transfer function of the tracking error will be applied to estimate the tracking error for the periodic disturbance. According to Fig. 6, the pulse transfer function of the tracking error ( $G_e(z)$ ) can be expressed as

$$G_e(z) = \frac{E(z)}{f(z)} = \frac{Q_2(z)}{1 + G'_2(z) Q_1(z)} \quad (25)$$

where  $f(z)$  represent the periodic disturbance that exists in the lumped disturbance.

According to the internal model principle [27], substituting  $z = e^{jm\omega_{in}t\omega}$ , ( $m = 1, 2, \dots, n$ ) into (25), the pulse transfer function of the tracking error can be rewritten as

$$G_e(e^{jm\omega_{in}t\omega}) = \frac{Q_2(e^{jm\omega_{in}t\omega})}{1 + G'_2(e^{jm\omega_{in}t\omega}) Q_1(e^{jm\omega_{in}t\omega})} \quad (26)$$

where  $\omega_{in}$  is the angular velocity of the input periodic signal.

Because the pulse transfer function in (26) is located in the complex plane, the absolute value  $|G_e(e^{jm\omega_{in}t\omega})|$  can be calculated to evaluate the tracking error of the periodic disturbance with the different angular velocity  $\omega_{in}$ . Based on (23) and (26), it can be seen that the absolute value is associated with the parameters  $\omega_{ob}$ ,  $K_r^m$ , and  $\omega_c^m$ . Apart from  $\omega_c^m$  that is set to 1.5% ( $m\omega_e$ ), the value of  $|G_e(e^{jm\omega_{in}t\omega})|$  can be drawn in Fig. 9 with the different  $\omega_{ob}$  and  $K_r^m$ , and the  $\omega_{in}$  is varies from 0 rad/s to 141.37 rad/s. The red lines in Fig. 9 denote the angular velocity  $\omega_{in}$  matches the resonant frequency of the designed QRC, which will have a smaller tracking error. Besides, Fig. 9(b) shows that a larger  $\omega_{ob}$  can reduce the tracking error while the sensitivity to the measurement noise will be greater, which will affect the observed performance. Therefore,

**Table 1**  
Hardware parameters and controller factors.

Symbol	Quantity	Value	Symbol	Quantity	Value
$P_r$	Rated power	5.5 kW	$\psi_f$	Permanent magnet flux	0.29 Wb
$S_r$	Rated speed	250 rpm	$R_s$	Stator resistance	0.675 $\Omega$
$I_r$	Rated current	7 A	$L_s$	Stator inductance	0.0065 H
$T_n$	Rated Load	6 N m	$J$	Rotational inertia	0.0425 kg m <sup>2</sup>
$n_p$	Number of pole pairs	3	$B$	Friction coefficient	0.02 N m s
$t_\omega$	Speed-loop sampling period	1 ms	$t_s$	Current-loop sampling period	100 $\mu$ s

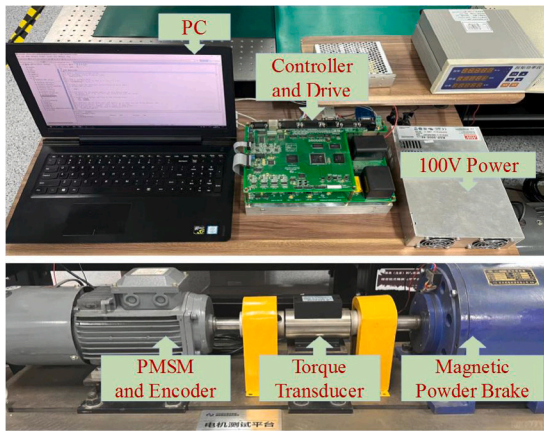


Fig. 10. Hardware platform system for PMSM.

there is a trade-off between the performance and the sensitivity. In our study, the  $\omega_{ob}$  is set to 200. Besides, a larger  $K_r^m$  will increase the gain that close to the resonant frequency, and improve the suppression performance of the periodic disturbance. Therefore, the  $K_r^1$  is set to 100, and  $k_r^2$  and  $k_r^6$  are set to  $2k_r^1$  and  $6k_r^1$ .

## 5. Experimental results

To test the feasibility of the proposed cascaded MFPS-C-QRC strategy, comparative experiments are implemented in a PMSM hardware system that integrates an FPGA into a TMS320-F28335 (DSP), as shown in Fig. 10, and the hardware and controller parameters are listed in Table 1. For the hardware system, the digital signal processor (DSP-TMS320F28335) is the core component that can process the controller code and generate the control command. As shown in Fig. 1, a cascaded structure will be applied to drive the PMSM. In the following experiments, the conventional PI control with a reference filter (PI-RF), the conventional model-based predictive speed control (MBPSC) [20], and the proposed MFPS-C-QRC are performed in the speed-loop. To ensure a fair comparison between the three strategies, the controller of the current-loop applies the FCS-MFPC strategy that is elaborated in Section 3.1. For the conventional PI control, a reference filter [28] is embedded to decrease the speed overshoot, and the filter time constant of the reference filter is set to 0.1 by balancing the response time and speed drop of the PI controller. The reference filter is designed in the discrete-time as

$$\omega_{m,ref}^k = \frac{t_{RF}}{t_\omega + t_{RF}} \omega_{m,ref}^{k-1} + \frac{t_\omega}{t_\omega + t_{RF}} \omega_m^* \quad (27)$$

where  $\omega_{m,ref}^k$  and  $\omega_{m,ref}^{k-1}$  denote the reference speed that is used in the speed-loop controller at ( $k$ )th and ( $k-1$ )th sampling period;  $\omega_m^*$  denotes the set reference speed. According to [29], the parameters  $K_p$  and  $K_i$  in the PI controller are selected as 0.1 and 0.6 by taking the rise time and speed drop into account. For the conventional MBPSC strategy, the parameters are determined based on the nominal value. In the proposed MFPS-C-QRC strategy, the scaling factor  $\alpha_\omega$  is determined by trial and error to minimize the speed tracking error, which is set to 35. Besides, the parameters of the QRC in our study are determined to  $K_r^1 = 100$ ,

$K_r^m = mK_r^1$ ,  $\omega_c^m = 1.5\% (m\omega_e)$ ,  $\omega_{ob} = 200$ , and the reference speed is to 50 rpm.

### 5.1. Periodic disturbance suppression performance

This section compares the steady-state performance of the PI-RF, conventional MBPSC, and the proposed MFPS-C-QRC strategy. The reference speed is set to 50 rpm. To make the comparison more intuitive, a periodic disturbance is added to the control system. The expression for the periodic disturbance is  $d(t) = 0.2 \sin(\omega_e t) + 0.1 \sin(2\omega_e t)$ . Figs. 11 and 12 show the experimental results of the speed tracking performance, current response, and Fast Fourier Transform (FFT) analysis of the speed. Because the load torque is categorized as the aperiodic disturbance, the 50% rated load and 100% rated load are applied in Figs. 11 and 12, respectively.

As shown in Fig. 11(a) and (b), the periodic disturbance will cause the motor speed to fluctuate. Because a Kalman filter is applied to observe the load and disturbance, the speed fluctuation of the conventional MBPSC strategy is 4.27 rpm, which is smaller than the 5.16 rpm of the conventional PI-RF. On the contrary, with the help of the designed QRC, the periodic disturbance in the proposed strategy can be effectively suppressed, the speed fluctuation can be reduced to 3.29 rpm, and the current fluctuation is reduced from 1.10 A to 0.68 A. Apart from the speed fluctuation in the time domain, the FFT results in the frequency domain also indicate that the proposed MFPS-C-QRC can effectively lower the speed harmonics. Especially for the first harmonic, the proposed MFPS-C-QRC strategy can reduce it from 1.51% to 0.18%. Meanwhile, the total harmonic distortion (THD) can also be effectively decreased from 2.41% to 1.42%, which is reduced by 41.08%. A similar performance of the periodic disturbance suppression is shown in Fig. 12 when the load torque is 100% rated load. To compare the suppression performance more intuitively, Fig. 13 shows the histogram of the speed fluctuation and THD for the three strategies. In the proposed MFPS-C-QRC strategy, an improved parallel quasi-resonant controller (QRC) is embedded into the MFPS-C strategy, which can simultaneously suppress the aperiodic and periodic disturbance. Therefore, the proposed MFPS-C-QRC strategy has a smaller speed fluctuation and lower THD.

### 5.2. Dynamic performance comparison

One of the advantages of model predictive control is its excellent dynamic performance. Therefore, the experiments are implemented under the motor starts and the load steps to verify the dynamic performance of the proposed MFPS-C-QRC strategy. The comparison results are shown in Fig. 14. For a more intuitive comparison, three metrics are chosen to compare the dynamic performance of the three strategies, as shown in Fig. 15.

Compared with the conventional PI-RF strategy, the rise time of the proposed MFPS-C-QRC strategy is reduced from 0.65 s to 0.38 s, which is decreased by 41.54%. For the conventional PI-RF strategy, with the help of a reference filter, the speed overshoot will be reduced, which can shorten the rise time, as shown in Fig. 14. However, the setting time of the conventional PI-RF strategy is 1.12 s, which is larger than the rise time. Benefiting from the excellent dynamic performance of the MPC, the proposed MFPS-C-QRC strategy can quickly respond to the load step, and the setting time only needs 0.35 s, which is decreased by

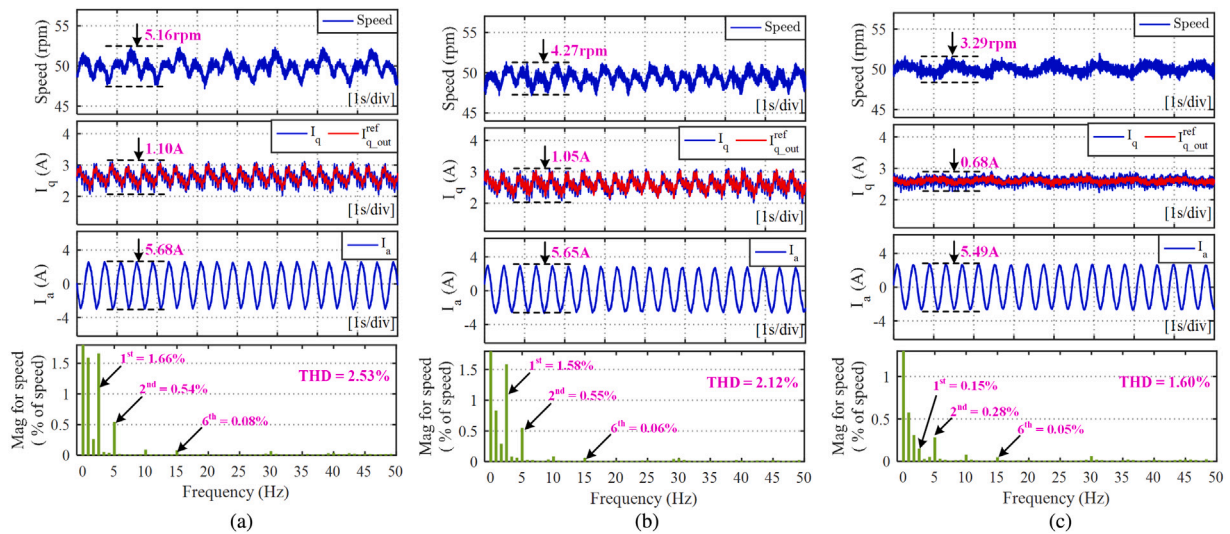


Fig. 11. Experimental results of the speed ripple suppression performance, current response, and speed FFT analysis at steady state with the reference speed 50 rpm and 50% rated load. (a) Conventional PI-RF; (b) Conventional MBPSC; (c) Proposed MFPSC-QRC.

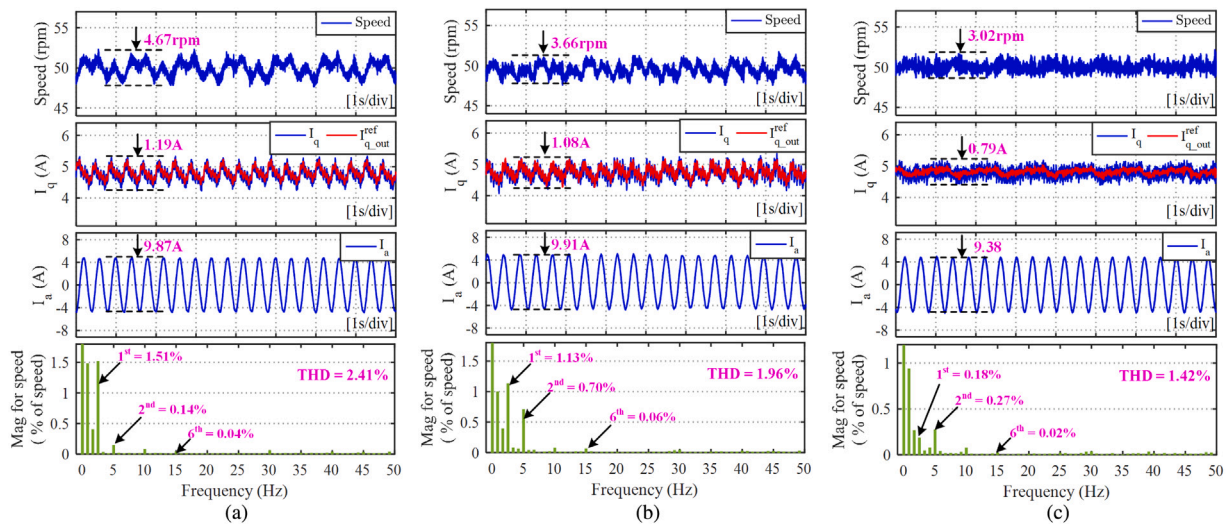


Fig. 12. Experimental results of the speed ripple suppression performance, current response, and speed FFT analysis at steady state with the reference speed 50 rpm and 100% rated load. (a) Conventional PI-RF; (b) Conventional MBPSC; (c) Proposed MFPSC-QRC.

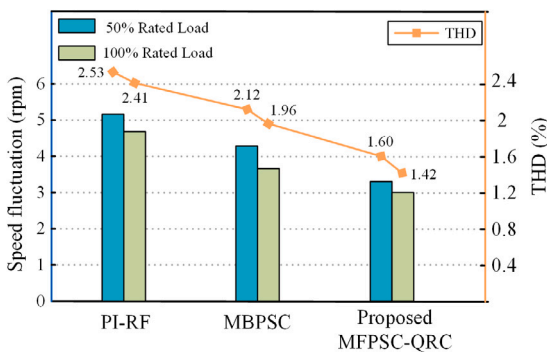


Fig. 13. The histogram of the speed fluctuation and THD under 50% rated load and 100% rated load for different methods.

68.75%. Furthermore, Fig. 14 demonstrates that the proposed MFPSC-QRC strategy can achieve a smaller speed drop than the conventional PI-RF strategy, which is only 2.48 rpm. Therefore, it can be seen more

obviously from Fig. 15 that the proposed MFPSC-QRC strategy not only has a rapid response speed and shorter recovery time but also can reduce the speed drop when the load steps.

### 5.3. Comparison results of parameters mismatch

For the conventional MBPSC strategy, since the controller depends on the motor parameters, the accuracy of the  $q$ -axis reference current may be affected if the actual values mismatch the nominal values. To verify the robustness of the designed CCS-MFPSC controller, a comparative experiment is implemented under the parameters mismatch. For the conventional MBPSC strategy, the values of the parameters are selected as 80% of the nominal values. In our study, the scaling factor  $\alpha_\omega$  will be varied to mimic the parameter mismatch.

Figs. 16 and 17 show the experimental results of the speed and current response under parameters mismatch. Each picture contains two stages: Stage I and Stage II. At stage I, the selected parameters use the nominal values, and the parameters value is selected to be 80% of the nominal value at stage II. Fig. 16 shows that the parameters mismatch will influence the speed tracking performance, especially for

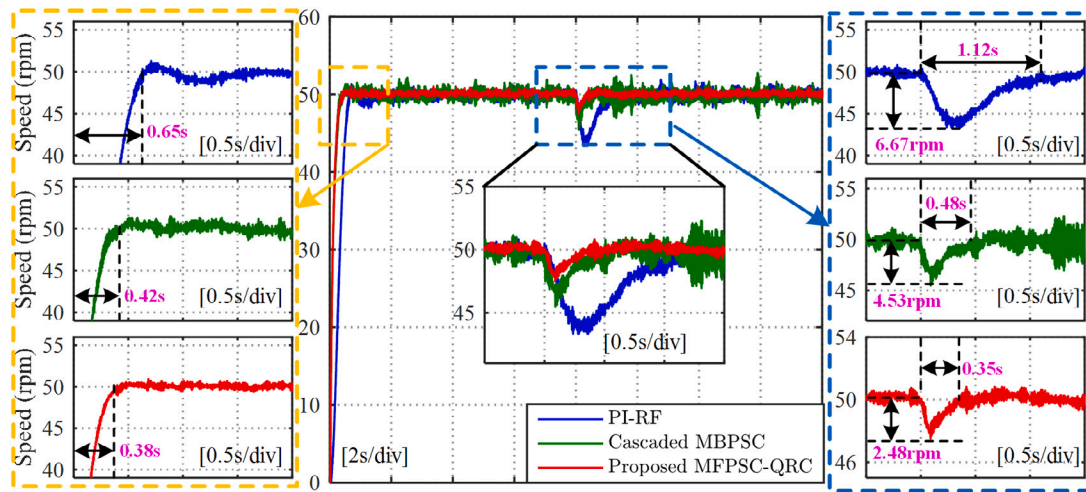


Fig. 14. Speed response of the three control strategies with the reference speed 50 rpm and the load steps from 0 N m to 3 N m.

Table 2  
Computational burden comparison.

Control methods	Speed-Loop			Current-Loop
	Main algorithm	Observer/Filter	QRC	FCS-MFPCC
PI-RF	0.36 $\mu$ s (55)	0.28 $\mu$ s (42)	None	31.19 $\mu$ s (4679)
Conventional MBPSC	2.25 $\mu$ s (338)	9.15 $\mu$ s (1373)	None	31.19 $\mu$ s (4679)
Proposed MFPS-C-QRC	1.96 $\mu$ s (294)	0.58 $\mu$ s (87)	16.89 $\mu$ s (2534)	31.19 $\mu$ s (4679)

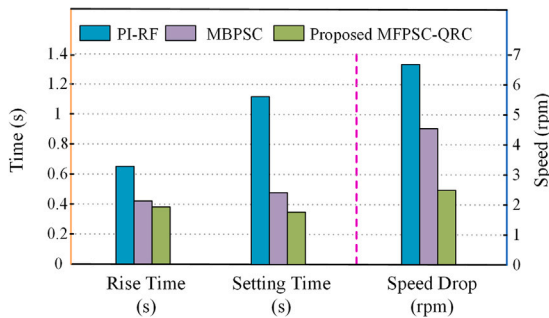


Fig. 15. The histogram of the speed response with the load steps.

the conventional MBPSC strategy. The speed fluctuation is increased from 2.47 rpm to 2.91 rpm, and the current fluctuation is increased from 0.79 A to 0.96 A. In contrast, with an ultra-local model, the proposed MFPS-C-QRC strategy can cast off the dependence on motor parameters. If the parameters mismatch, the speed fluctuation can be reduced from 2.91 rpm to 2.17 rpm. Furthermore, the FFT analysis results and the histogram can show more intuitively that the proposed strategy has smaller speed harmonics and lower THD in the frequency domain, which means that the proposed MFPS-C-QRC strategy has stronger robustness.

#### 5.4. Computational burden comparison

In the conventional FCS-MPC strategy, the optimal actuation can be selected by iterating through all the possible results, which will increase the computational burden. Therefore, it is necessary to calculate the computational time to guarantee that the proposed strategy can be effectively implemented on the hardware platform. The computational time that is calculated based on the number of clock cycles of a DSP is listed in Table 2. In our experimental platform, the main-frequency of the DSP (TMS320F28335) is 150 MHz, which means that each clock cycle of the DSP is 1/150  $\mu$ s. The numbers in parentheses in Table 2

represent the clock cycles required to execute this program. Finally, the computational time is calculated by multiplying the clock cycles by 1/150  $\mu$ s.

To fairly compare the performance of the speed loop controller, the current-loop controller of the three strategies is the FCS-MFPCC strategy that needs 31.19  $\mu$ s. For the speed-loop controller, the computational time of the conventional PI is the smallest, which only needs 0.36  $\mu$ s. However, the steady-state and dynamic performance of the MPC is more excellent than the conventional PI controller. For the conventional MBPSC strategy, because the derivation of the  $q$ -axis reference current needs a complex computational formula, the computational time is larger than the proposed MFPS-C strategy, which is increased from 1.96  $\mu$ s to 2.25  $\mu$ s. Besides, an observer is necessary for the predictive speed control to estimate the load and lumped disturbance, which only needs 0.58  $\mu$ s. Furthermore, because a parallel quasi-resonant controller (QRC) is embedded into the CCS-MFPSC, the computational time of the proposed MFPS-C-QRC strategy will be increased by 16.89  $\mu$ s. Based on the designed ESO and QRC, the aperiodic disturbance and periodic disturbance can be effectively suppressed. Although the computational time of the proposed MFPS-C-QRC strategy is longer, the dynamic performance and the disturbance suppression performance can be significantly improved.

#### 6. Conclusion

To achieve a smooth speed, this paper studies an improved cascaded model-free predictive speed and current control strategy. The current-loop controller is the FCS-MFPCC strategy, and a CCS-MFPSC strategy is proposed in the speed loop to take full advantage of the excellent dynamic performance of the current-loop controller. Meanwhile, an improved parallel quasi-resonant controller (QRC) is embedded into the CCS-MFPSC strategy to simultaneously suppress the aperiodic and periodic disturbances. The stability of the proposed MFPS-C-QRC strategy and the parameters selection for the QRC are analyzed systematically. Besides, the proposed MFPS-C-QRC strategy is implemented on

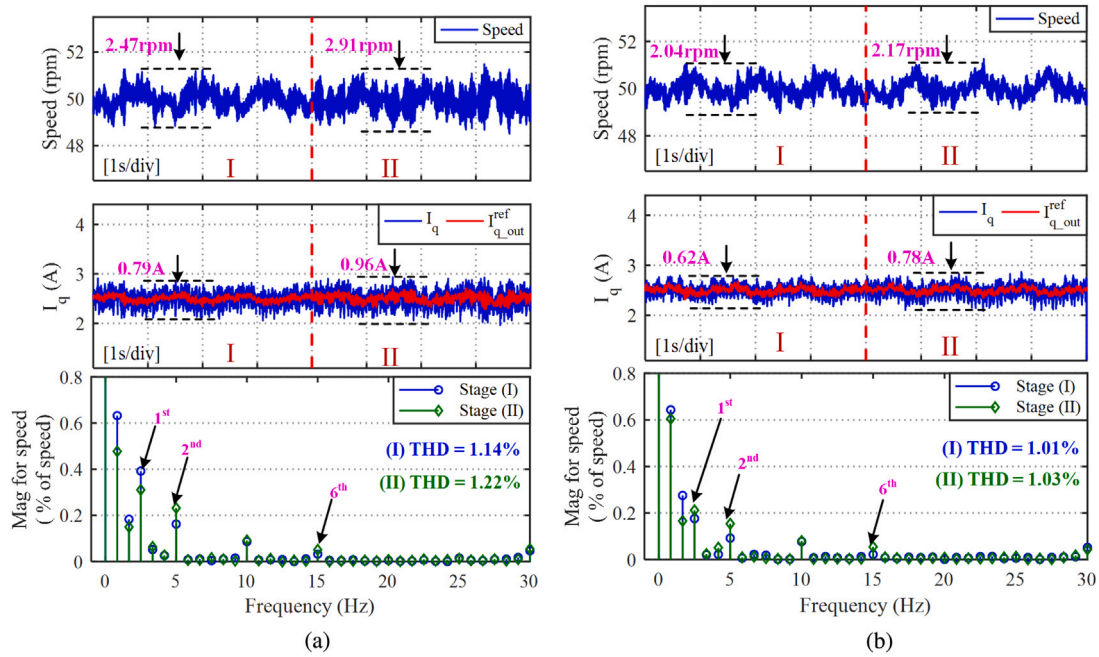


Fig. 16. Experimental results of the speed and current response and speed FFT analysis at steady state under parameters mismatch. (a) Conventional MBPSC; (b) Proposed MFPPSC-QRC.

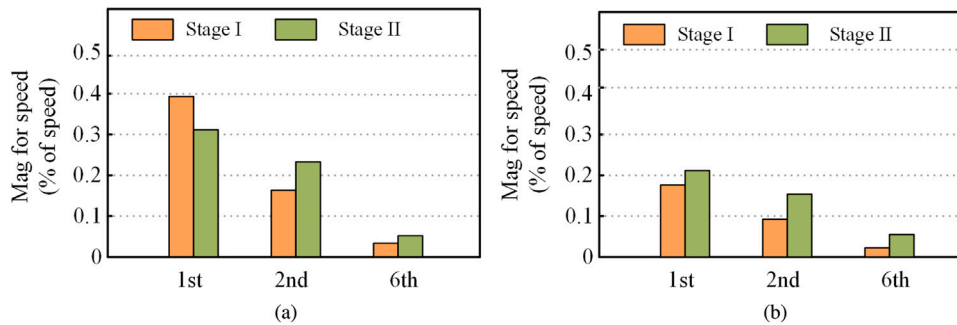


Fig. 17. The histogram of the FFT analysis for the speed response under the parameters mismatch. (a) Conventional MBPSC; (b) Proposed MFPPSC-QRC.

the PMSM hardware system to verify its feasibility and practicability. The experimental results demonstrate that the proposed MFPPSC-QRC strategy exhibits excellent steady-state speed tracking and dynamic performance. Compared with the conventional PI with reference filter and the conventional MBPSC strategy, the proposed MFPPSC-QRC strategy can effectively decrease the speed fluctuation and suppress the aperiodic and periodic disturbances. Furthermore, the proposed MFPPSC-QRC strategy has stronger robustness when the motor parameter mismatches. According to the experimental results, the conclusion can be drawn that the proposed MFPPSC-QRC strategy not only has excellent dynamic performance but also can effectively suppress the periodic and aperiodic disturbances simultaneously.

**Declaration of competing interest**

The authors declare that they have no known competing financial interests or personal relationships that could have appeared to influence the work reported in this paper.

**Acknowledgments**

This work was supported by the National Nature Science Foundation of China (Grant no. 11973041 and 12122304), Youth Innovation Promotion Association, Chinese Academy of Science, China (Grant no. 2019218).

**References**

- [1] Cao H, Deng Y, Li H, Wang J, Liu X, Sun Z, Yang T. Generalized active disturbance rejection with reduced-order vector resonant control for PMSM current disturbances suppression. *IEEE Trans Power Electron* 2023;38(5):6407–21.
- [2] Deng Y, Wang J, Li H, Liu J, Tian D. Adaptive sliding mode current control with sliding mode disturbance observer for PMSM drives. *ISA Trans* 2019;88:113–26.
- [3] Liu J, Li H, Deng Y. Torque ripple minimization of PMSM based on robust ILC via adaptive sliding mode control. *IEEE Trans Power Electron* 2018;33:3655–71.
- [4] Houari A, Bouabdallah A, Djerioui A, Machmoum M, Auger F, Darkawi A, Olivier J-C, Benkhoris MF. An effective compensation technique for speed smoothness at low-speed operation of PMSM drives. *IEEE Trans Ind Appl* 2018;54(1):647–55.
- [5] Rodríguez J, Pontt J, Silva CA, Correa P, Lezana P, Cortes P, Ammann U. Predictive current control of a voltage source inverter. *IEEE Trans Ind Electron* 2007;54(1):495–503.
- [6] Ahmed AA, Koh BK, Lee YI. A comparison of finite control set and continuous control set model predictive control schemes for speed control of induction motors. *IEEE Trans Ind Inf* 2018;14(4):1334–46.
- [7] Siami M, Khaburi DA, Rodríguez J. Torque ripple reduction of predictive torque control for PMSM drives with parameter mismatch. *IEEE Trans Power Electron* 2017;32(9):7160–8.
- [8] Yao Y, Huang Y, Peng F, Dong J, Zhang H. An improved deadbeat predictive current control with online parameter identification for surface-mounted PMSMs. *IEEE Trans Ind Electron* 2020;67(12):10145–55.
- [9] Wang B, Chen X, Yu Y, Wang G, Xu D. Robust predictive current control with online disturbance estimation for induction machine drives. *IEEE Trans Power Electron* 2017;32(6):4663–74.

- [10] Yuan X, Zuo Y, Fan Y, Lee CHT. Model-free predictive current control of SPMSM drives using extended state observer. *IEEE Trans Ind Electron* 2022;69(7):6540–50.
- [11] Zhang X, Hou B, Mei Y. Deadbeat predictive current control of permanent-magnet synchronous motors with stator current and disturbance observer. *IEEE Trans Power Electron* 2017;32(5):3818–34. <http://dx.doi.org/10.1109/TPEL.2016.2592534>.
- [12] Lin C-K, Liu T-H, Yu J-t, Fu L-C, Hsiao C-F. Model-free predictive current control for interior permanent-magnet synchronous motor drives based on current difference detection technique. *IEEE Trans Ind Electron* 2014;61(2):667–81.
- [13] Lin C-K, Yu J-t, Lai Y-S, Yu H-C. Improved model-free predictive current control for synchronous reluctance motor drives. *IEEE Trans Ind Electron* 2016;63(6):3942–53.
- [14] Sun Z, Deng Y, Wang J, Yang T, Wei Z, Cao H. Finite control set model-free predictive current control of PMSM with two voltage vectors based on ultralocal model. *IEEE Trans Power Electron* 2023;38(1):776–88.
- [15] Zuo Y, Zhu X, Quan L, Zhang C, Du Y, Xiang Z. Active disturbance rejection controller for speed control of electrical drives using phase-locking loop observer. *IEEE Trans Ind Electron* 2019;66(3):1748–59.
- [16] Yang T, Deng Y, Li H, Sun Z, Cao H, Wei Z. Fast integral terminal sliding mode control with a novel disturbance observer based on iterative learning for speed control of PMSM. *ISA Trans* 2023;134:460–71.
- [17] Muramatsu H, Katsura S. An adaptive periodic-disturbance observer for periodic-disturbance suppression. *IEEE Trans Ind Inform* 2018;14(10):4446–56.
- [18] Chen D, Zhang J, Qian Z. An improved repetitive control scheme for grid-connected inverter with frequency-adaptive capability. *IEEE Trans Ind Electron* 2013;60(2):814–23.
- [19] Pan Z, Dong F, Zhao J, Wang L, Wang H, Feng Y. Combined resonant controller and two-degree-of-freedom PID controller for PMSLM current harmonics suppression. *IEEE Trans Ind Electron* 2018;65(9):7558–68.
- [20] Garcia C, Rodriguez J, Silva C, Rojas C, Zanchetta P, Abu-Rub H. Full predictive cascaded speed and current control of an induction machine. *IEEE Trans Energy Convers* 2016;31(3):1059–67.
- [21] Wang B, Tian M, Yu Y, Dong Q, Xu D. Enhanced ADRC with quasi-resonant control for PMSM speed regulation considering aperiodic and periodic disturbances. *IEEE Trans Transp Electr* 2022;8(3):3568–77.
- [22] Trinh QN, Wang P, Tang Y, Koh LH, Choo FH. Compensation of DC offset and scaling errors in voltage and current measurements of three-phase AC/DC converters. *IEEE Trans Power Electron* 2018;33(6):5401–14.
- [23] Fliess M, Join C. Model-free control. *Int J Control* 2013;86:2228–52.
- [24] Zhang Y, Jin J, Huang L. Model-free predictive current control of PMSM drives based on extended state observer using ultralocal model. *IEEE Trans Ind Electron* 2021;68(2):993–1003.
- [25] Yepes AG, Freijedo FD, Doval-Gandoy J, Lopez O, Malvar J, Fernandez-Comesana P. Effects of discretization methods on the performance of resonant controllers. *IEEE Trans Power Electron* 2010;25(7):1692–712.
- [26] Xia C, Ji B, Yan Y. Smooth speed control for low-speed high-torque permanent-magnet synchronous motor using proportional-integral-resonant controller. *IEEE Trans Ind Electron* 2015;62(4):2123–34.
- [27] Francis B, Wonham W. The internal model principle of control theory. *Automatica* 1976;12(5):457–65.
- [28] Vrancic D, Strmcnik S, Kocijan J, de Moura Oliveira P. Improving disturbance rejection of PID controllers by means of the magnitude optimum method. *ISA Trans* 2010;49(1):47–56.
- [29] Harnefors L, Saarakkala SE, Hinkkanen M. Speed control of electrical drives using classical control methods. *IEEE Trans Ind Appl* 2013;49(2):889–98.